TH-2025-11-0177

A Direction-Dependent Mechanotransduction Model to Convert Fingertip Forces into Neural Spike Trains for Tactile Feedback

Hope O. Shaw, John McBride, and Liudi Jiang

Abstract— **Microneurography studies have shown that human mechanoreceptor (MR) activity is directionally sensitive to shear forces, enabling fine tactile perception and object manipulation. However, existing computational mechanotransduction models largely neglect this directional tuning, limiting their biological realism and effectiveness for tactile feedback systems such as prosthetic hands. This paper presents a Direction-Dependent Mechanotransduction Model (DDMM) that replicates the direction-specific encoding behavior observed in human tactile afferents. The model integrates multidirectional pressure and shear forces to modulate neural spiking according to the alignment between resultant shear vectors and neuron-specific attenuation profiles. Force inputs are first transformed into afferent-specific currents (SAI, RAI, RAII), which are then converted into spike trains using an Izhikevich neuron model. Simulated fingertip interactions produced directionally selective spiking frequencies ranging from 0 to 47.5 pulses per second, consistent with biological firing ranges. Directional tuning, quantified using the profile-resolved sensitivity index (PRSI), yielded values of 0.31–0.45 for selective and broad profiles, comparable with those experimentally measured directional sensitivity indices (DSI; 0.23 ± 0.18) as reported in the literature. Further experimental validation using triaxial force measurements from human fingertip press–push–lift actions confirm the model's directional sensitivity, with aligned neural attenuation profiles and shear force direction yielding a mean spiking frequency increase of approximately 350% relative to misaligned conditions. These findings establish the DDMM as a biologically inspired and computationally efficient framework for encoding tactile force direction, with potential applications in neuroprosthetics, robotic manipulation, and somatosensory modeling.**

I. INTRODUCTION

Tactile sensation in human hands is communicated to the brain as neural spike trains through mechanoreceptors (MR) which are embedded in the glabrous skin of the fingertips [1]. Cutaneous MRs are typically categorized into four main types based on adaptation rate and receptive field characteristics. Slow Adapting Type I (SAI) receptors are slow to adapt with a small, precisely bound area of sensitivity [2]. They are stimulated by direct pressure and fire at a frequency that is directly proportional to the magnitude of the applied force. The high density of SAI receptors in the fingertip allows multiple neighboring receptors to work in unison to detect edges and track movement [3]. Slow Adapting Type II (SAII) receptors sit deeper in the dermis than SAI receptors. They maintain the slow adapting response of SAI receptors but have a broader area of sensitivity with blurred boundaries. SAII receptors have been reported to fire during skin stretch, contributing to proprioception such as detecting skin deformation during finger movements [4]. Other receptors include Rapid Adapting Type I (RAI) receptors, responding to dynamic changes in pressure and thus are sensitive to low frequency vibrations, and Rapid Adapting Type II (RAII) receptors which fire during acceleration of pressure and thus are sensitive to high frequency vibrations [2, 5].

There has been considerable research interest in computational models that simulate the transduction mechanisms of MRs embedded in the human hand [6]. These models are critical for developing realistic tactile feedback at human-computer, human-machine and fingertip-object interfaces. For instance, practical implementation of these models could offer promising tactile feedback solutions for prosthetic hand users or patients with sensory losses caused by e.g. peripheral neuropathy [6-8]. Specifically, signals from fingertip force sensors mounted on prosthetic fingertips could be converted into neural spike trains that mimic those generated by MRs. These spike trains could then be transmitted via nerves through invasive neurostimulation techniques, such as implanted electrodes [9, 10], ultimately enabling the brain to process them as if they were natural neural signals. This would not only provide prosthesis users with a realistic sensation of touch, but also potentially enable closed-loop control of the prosthesis, paving the way for more intuitive functions in future artificial hands.

During activities of daily living, the fingertip experiences a range of complex multi-directional forces while touching surfaces or handling objects. These forces can be decomposed into applied forces, (perpendicular to the contact surface), and shear forces (tangential to the contact surface) [11]. Several computational MR models have been reported to date, with the majority using uni-axial force i.e. only applied force [12]. Models incorporating shear forces have focused mainly on texture discrimination and edge detection [13-15], using techniques such as population coding and deep learning. Valero et al [16] reported a comprehensive mechanotransduction model with multidirectional pressure and shear force inputs measured by Tri-Axial Pressure and Shear (TRIPS) sensors, leading to the generation of spike trains. Although pressure and

This research was funded by the UK Engineering and Physical Sciences Research Council (EPSRC) Grant EP/S02249X/1 for the Center for Doctoral Training in Prosthetics and Orthotics. Corresponding author: H. Shaw and L. Jiang

The authors are with the School of Engineering, University of Southampton, Southampton SO17 1BJ, UK (e-mail: hos1n15@soton.ac.uk; l.jiang@soton.ac.uk).

shear forces were independently recorded in this case, the MR model has simply used the resultant pressure and shear forces which was used as the model input.

Several studies [3, 17, 18] have reported that the spike trains recorded from SAI, and SAII and RAI afferents in natural hands were sensitive to the directions of the externally applied forces. SAII afferents were excluded from this study because their responses primarily reflect skin stretch and hand posture during manipulation rather than dynamic contact force encoding, and their firing cannot be reliably inferred from measured fingertip interface forces alone. Research on primate somatosensory cortex [19] revealed that approximately half of the recorded afferents showed directional tuning. Different neural responses have been recorded depending on the direction of a force stimuli applied tangentially across the skin surface i.e. shear force [18]. Directional tuning represents a fundamental property of MRs that is essential for tactile perception. Pioneering microneurography studies by Birznieks et al. [3] revealed that, when changing the shear force angle within the plane of the skin surface, while maintaining pressure, many of the recorded afferents (SAI, SAII and RAI) exhibited distinct directional tuning profiles. Approximately 86% of afferents showed statistically significant directional preference, implying that directional sensitivity is not merely an occasional feature but rather a dominant characteristic of tactile encoding. They also revealed that each afferent had an optimal shear force angle at which neural firing rates were highest. Thus, incorporating shear force angles as indicators of direction is critical for accurately representing neural activities and should be implemented in mechanotransduction models to replicate the direction-dependent behavior of cutaneous MRs. No such model has been reported to date.

This study presents a novel direction-dependent mechanotransduction model that incorporates shear force angle as a critical factor, enabling the generation of neural spikes that replicate the tuning effects observed in MR afferents. Initially the model was evaluated by comparing to previously reported biological recordings. The model's performance was then evaluated by inputting purposely designed forces with specific directions simulating fingertip press-push-lift actions. The resulting neural activities and their variation with shear force angles were analysed as compared with those reported from human MR afferents. Subsequently, typical multidirectional fingertip forces were experimentally measured during fingertip press-push-lift actions from a human participant. This serves as a pilot validation of the model's effectiveness in generating spike trains that mimic those of human cutaneous MRs.

II. RELATED WORK

A. Mechanotransduction model for neural spiking

Mechanotransduction is typically modelled in two stages as illustrated in Fig. 1, referred to as the conventional mechanotransduction model (CMM).

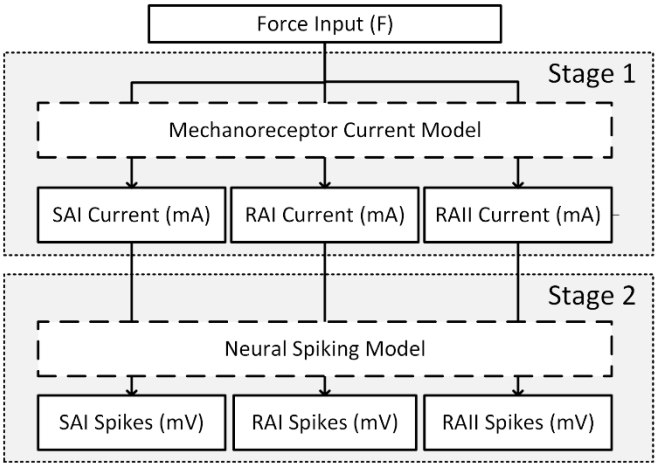

Fig. 1- Two-stages of a conventional mechanotransduction model (CMM)

In Stage 1, the MR model takes a fingertip force input (F) to generate corresponding afferent currents which simulate the dynamic behavior of SAI, RAI, and RAII afferents. It is known that SAI afferents directly respond to force [20], RAI afferents respond to changes in force [4], and RAII afferent group are reported to respond to accelerations at the finger-surface interface [2, 4]. Thus, their respective currents can be modelled as functions of F as shown in Equations (1)-(3).

$$I_{SAI} \approx n \cdot |F| \tag{1}$$

$$I_{RAI} \approx \left(\frac{d}{dt}|F|\right) \tag{2}$$

$$I_{RAII} \approx \left(\frac{d^2}{dt^2}|F|\right) \tag{3}$$

Subsequently in Stage 2, these currents are fed into neural spiking model to convert into corresponding spike trains, whereby the Izhikevich neuron model has been commonly used [21-24] due to its effectiveness [21], and being computationally efficient [22]. The model is defined by Equations (4)-(6), where v represents the voltage potential and u represents the membrane recovery. The parameters of A, B, C and D are defined to characterize the model's firing responses for SAI, RAI and RAII. Parameter A was fixed at 0.02 for all afferent types, setting the time scale of the recovery variable. The post-spike reset potential was held constant at $C = -65$, while $D = 8$ governed the post-spike increment of the recovery variable and therefore spike-frequency adaptation. In contrast, parameter B, which controls sensitivity to subthreshold membrane potential, varied across afferent types. RAI ($B = 0.25$) and RAII ($B = 0.25$) afferents were modelled as low-threshold spiking (LTS) neurons, reflecting their heightened responsiveness to small depolarizations, whereas SAI afferents were modelled as regular spiking (RS) neurons ($B = 0.20$), consistent with their more sustained firing behavior. The variable I represents synaptic or injected currents, and for the following work is typically set to 0.

$$\frac{dv}{dt} = 0.04v^2 + 5v + 140 - u + I \quad (4)$$

$$\frac{du}{dt} = A \cdot ((B \cdot v) - u) \quad (5)$$

$$if\ v \geq 30, \text{ then } \begin{cases} v \leftarrow C \\ u \leftarrow u + D \end{cases} \quad (6)$$

B. Directional-Tuning Observed in Microneurography Recordings

Microneurography studies have been reported to record neural impulses. For example, Birznieks et al. [3] recorded from 196 tactile afferents while participants' fingertips were subjected to five distinct force conditions: normal applied force only (kept at 4N) and four directional static forces applied at an incline of 20° from the normal force. They reported a fundamental directional tuning property with 93% of SAI, and 83% of RAI afferents. They also defined a directional sensitivity index (DSI) as shown in Equation 7, where r_θ represents the neural response to a stimulus at angle θ. Mean ± SD DSIs of ~0.23 ± 0.18 for SAI and ~0.24 ± 0.18 for RAI were reported for human tactile afferents during force application [3].

$$DSI = \frac{\sqrt{(r_0 - r_{180})^2 + (r_{90} - r_{270})^2}}{r_0 + r_{90} + r_{180} + r_{270}} \quad (7)$$

Fortier-Poisson et al. further demonstrated [17] direction-sensitivity to static shear forces in the activity of the somatosensory cortex. Approximately 85% of both slowly and rapidly adapting neurons were directionally sensitive to static shear forces, with the neural activity modulated by shear force directions. They have reported different shapes of neural attenuation profiles (NAPs), as shown by the dark-blue areas in Fig. 2. These blue shaded areas were produced based on biological neuro-recordings when shear forces with varied angles were applied at the fingertip. It thus illustrates the range of affecting shear force angles and corresponding magnitudes, essentially forming the NAPs.

C. Definition Assignment for NAPs

We introduce several angle definitions, as also shown in Fig. 2, including resulted shear angle $\theta_R(t)$, selectivity range (θ_A) denoting the angle range of shear forces that have a significant attenuation effect, and the tuning angle (θ_T) denoting the characteristic angle whereby maximum neural attenuation from shear forces is recorded, i.e. when $\theta_R(t) = \theta_T$. As $\theta_R(t)$ deviates from θ_T, reduction of shear modulation in neural activity can be observed, eventually leading to a sharp drop when $\theta_R(t)$ is out of θ_A. Specifically, three main types of

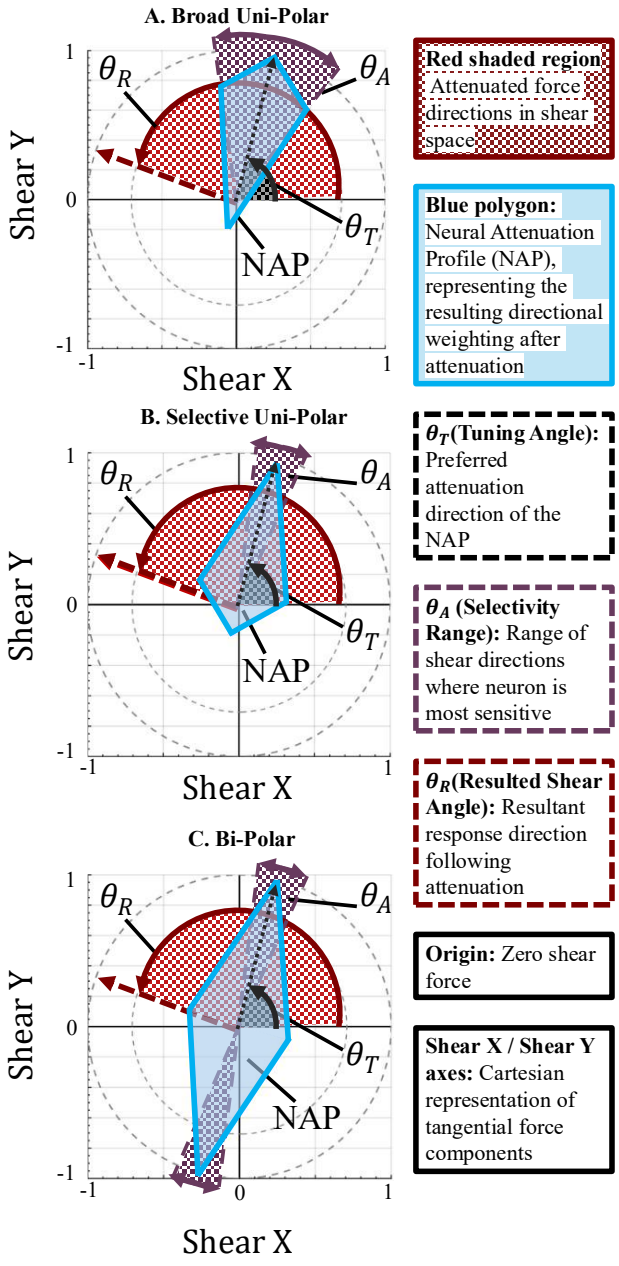

Fig. 2 - Broad uni-polar (A), selective uni-polar (B), and bi-polar (C) attenuation patterns in shear space representing concepts from [3,17]

NAPs were observed in microneurography experiments across slowly and rapidly adapting neurons [17]. Neurons with a low selectivity range (θ_A < 50°) demonstrated pronounced directional tuning, as illustrated in Fig. 2(b). This response NAP is hereafter referred to as Selective Uni-Polar. Some neurons exhibited responses across broader directions $50° < \theta_A < 170°$, as compared with selective uni-polar type. We therefore refer to Broad Uni-Polar NAP (Fig. 2(a)). Bi-polar behavior was also observed (Fig. 2(c)), where shear force angles in both positive and negative directions produced significant attenuations in neuro-recordings. This response NAP is thus named Bi-polar [17, 18].

III. Direction-Dependent Mechanotransduction Model (DDMM)

A: DDMM Principle

We herein report a DDMM whereby an attenuation factor ($AF(t)$) is introduced as indicated by Fig. 3. $AF(t)$ is obtained through the intersection of shear force with the corresponding NAP at $x_i(t), y_i(t)$, as shown in Fig. 4 for a typical broad uni-polar NAP.

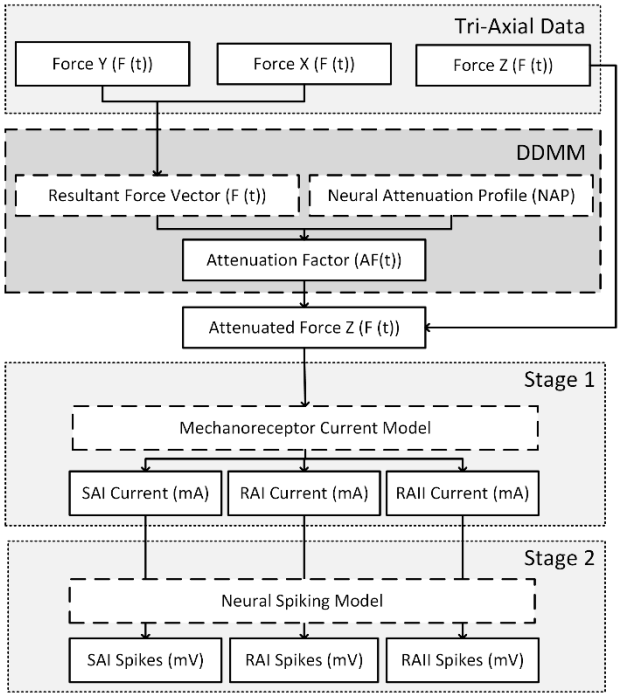

Fig. 3 - Direction-Dependent Mechanotransduction Model (DDMM) integrating the attenuation factor (AF) within the mechanotransduction pathway

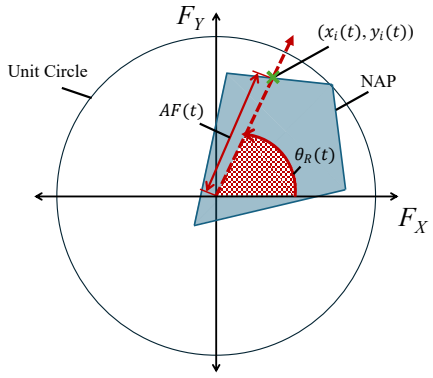

Fig. 4- Example of a resultant shear-force vector interacting with a broad uni-polar NAP to determine AF(t).

The AF(t) can then be coupled with applied force $F_Z(t)$ to produce attenuated force ($F_A(t)$), which replaces the direct force input in the conventional MR model (Fig. 1). The intersects of $x_i(t), y_i(t)$ in Fig. 4 can be calculated as:

$$y(t) = \frac{F_Y(t)}{F_X(t)} \cdot x(t) \tag{8}$$

where $F_X(t)$ and $F_Y(t)$ represent shear force in both the X and Y directions at a time t, respectively.

B: Parameters to define Neural Attenuation Profiles (NAP)

Equations (9 – 11) define the boundary for a NAP. The values of X and Y represent a rotation matrix, allowing the NAP to be rotated around the origin to accommodate different θ_T. Each of the three types of NAPs in Fig. 2 can be defined by assigning specific values to the parameters of p_1, p_2, p_3, p_4, and p_5, as shown in Fig. 5 so that NAPs can be achieved that align with those observed in biological studies [3,16-18]. These values are listed in Table I. A parameter k is also introduced as horizontal scaling factor, which is defined by the selectivity range θ_A following Equation (12).

$$p_1(|kX| + |p_2 Y - p_3| - p_4) - p_5 Y = 0, \tag{9}$$

where:

$$X = x\cos(\theta_T) + y\sin(\theta_T) \tag{10}$$

$$Y = -x\sin(\theta_T) + y\cos(\theta_T) \tag{11}$$

TABLE I- Neural attenuation profile (NAP) parameters

Profile	p_1	p_2	p_3	p_4	p_5
Bi-polar	1	1	0	1	0
Selective Uni-polar	1	2	0.2	0.8	1
Broad Uni-polar*	-1	2	1.2	1.4	1

* $k \geq 1.8$

$$k = \frac{b}{\tan\left(\frac{\theta_A}{2}\right)} \tag{12}$$

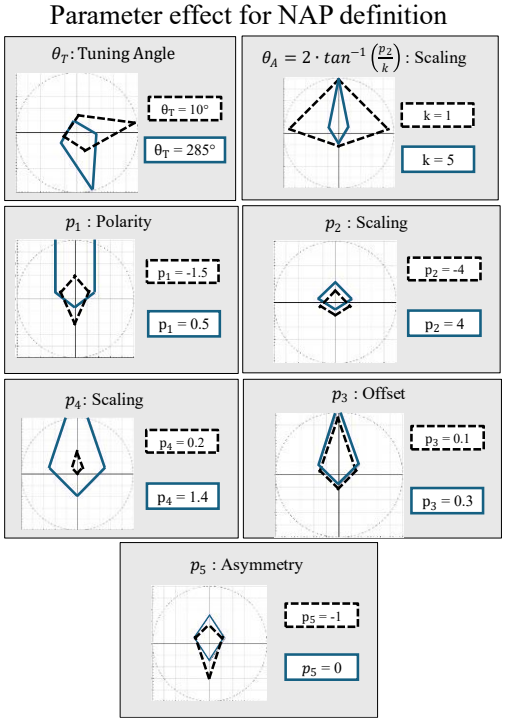

Fig. 5 – Parameter definitions and rotation matrix used for NAPs.

C: Attenuation Factor (AF(t)) and Attenuated Force ($F_A(t)$)

AF(t) is derived from the intersections with the NAP ($X_i(t)$, $Y_i(t)$) with details illustrated in Fig. 5. Specifically, when θ_R(t) = θ_T, we define AF(t) = 1, i.e.; $F_A(t) = F_Z(t)$; when $\theta_R(t) \neq \theta_T$, AF(t) < 1, suppressing the attenuated applied force i.e.; $F_A(t) < F_Z(t)$, resulting in reduced afferent currents and hence reduced neural spiking.

The co-ordinates $(x_i(t), y_i(t))$ can be derived by substituting Equation (8), into the NAP Equations (9 - (11), giving:

$$p_1(|kX| + |p_2Y - p_3| - p_4) - p_5Y = 0, \quad (13)$$

where:

$$X = x_i(t)\cos(\theta_T) + \left(\frac{F_Y(t)}{F_X(t)} \cdot x_i(t)\right)\sin(\theta_T) \quad (14)$$

$$Y = -x_i(t)\sin(\theta_T) + \left(\frac{F_Y(t)}{F_X(t)} \cdot x_i(t)\right)\cos(\theta_T) \quad (15)$$

Equation (13) can now be solved for $x_i(t)$, giving two solutions. This is due to the equation for resultant shear force vector, which creates a projection of the vector beyond the origin. To compensate for this, if the shear force has a positive value of $x(t)$ the positive solution for $x_i(t)$ is selected, otherwise the negative solution is selected. The value for $x_i(t)$ is then substituted into Equation (8), to give the corresponding solution for $y_i(t)$. Directional attenuation is applied only when the magnitude of the resultant shear force, $F_S(t)$, exceeds a small threshold (F_{TH}). When $F_{TH} = 0.1$, the stimulus is treated as effectively normal loading, and no directional attenuation is applied. Otherwise, attenuation factor $AF(t)$ can be defined using the $(x_i(t), y_i(t))$ coordinates, as shown by:

$$F_S(t) = \sqrt{F_X(t)^2 + F_Y(t)^2} \quad (16)$$

$$AF(t) = \begin{cases} 1, & F_S(t) \leq F_{TH} \\ \sqrt{x_i(t)^2 + y_i(t)^2}, & F_S(t) > F_{TH} \end{cases} \quad (17)$$

and thus, the attenuated applied force $F_A(t)$ is:

$$F_A(t) = AF(t) \cdot F_Z(t) \quad (18)$$

As shown in Fig. 3, $F_A(t)$ is then passed through the current and neural model to generate the resulting spike trains.

IV. Theoretical Evaluation of DDMM

A: Model Validation Based on Reported Physiological Data

A synthetic fingertip force dataset was constructed, as shown in Fig. 6(a), to match those reported by Birznieks et al. [3] with a view to comparing the DDMM outputs with their experimentally measured directional sensitivity. In particular, a constant normal force of 4N was applied and the synthetic dataset has the following stages:

- Stage 1 (0 to 0.125 second): Dynamic ramping up of contact forces.
- Stage 2 (0.125 to 0.375 second): Performing a static pushing along Y direction to generate $F_Y(t)$ and $F_Z(t)$, simultaneously, i.e. θ_R(t) = 90.
- Stage 3 (0.375 to 0.5 second): Dynamic ramping down of contact forces.

Analogous to the directional sensitivity index (Equation 7) [3], a profile-resolved sensitivity index (PRSI) is calculated using neural profiles with θ_T set at 90° intervals, allowing for comparison to the biological recorded DSI results. Akin to the DSI equation, S_{θ_T} represents the neural response of the model tuned to θ_T.

$$PRSI = \frac{\sqrt{(S_0 - S_{180})^2 + (S_{90} - S_{270})^2}}{S_0 + S_{90} + S_{180} + S_{270}} \quad (19)$$

Figure 6a shows the replicated force inputs, with each stage highlighted. Figure 6b-g show the resulting spike trains for each afferent produced by the NAP shown in Part IV. Two tuning angles, θ_T= 90° and 180°, are examined per NAP shape to represent true-alignment and true-unalignment conditions, respectively. A typical sensitivity value of k = 3 is used. Figure 6 b–g presents the resulting spike outputs as a time series and histograms to better visualize changing frequencies. To mirror the reported DSI values, PRSI was calculated for this output as shown in Table II.

TABLE II - PRSI under aligned and misaligned conditions compared with corresponding DSI values reported in [3].

	Selective	Broad	Bi	DSI
SAI	0.38	0.45	0	~0.23 ± 0.18
RAI	0.31	0.36	0	~0.24 ± 0.18
RAII	0.33	0.33	0	Not Reported

The PRSI values reported here (SAI: 0.38 and 0.45 for selective and broad profiles, respectively; RAI: 0.31 and 0.36) are comparable to the experimentally measured DSI values reported by Birznieks et al. (SAI: 0.23 ± 0.18; RAI: 0.24 ± 0.18) [3], falling within the first standard deviation of the biological data. The bipolar profile produced a PRSI of 0 across all afferent types, as it is calculated from diametrically opposed conditions in which the bipolar profile is identical and therefore cancels in the vector sum.

B: A Case Study of Diametrically Opposed Tuning Angles

The performance of the DDMM is evaluated by applying the three-dimensional artificial force input $F_X(t), F_Y(t), F_Z(t)$ (Fig. 7(a)) to the three NAP shapes: bi-polar, broad uni-polar, and selective uni-polar (Fig. 2). This artificial force was constructed to simulate real-world fingertip press-push-lift data. Due to difference in experimental capabilities, the stages

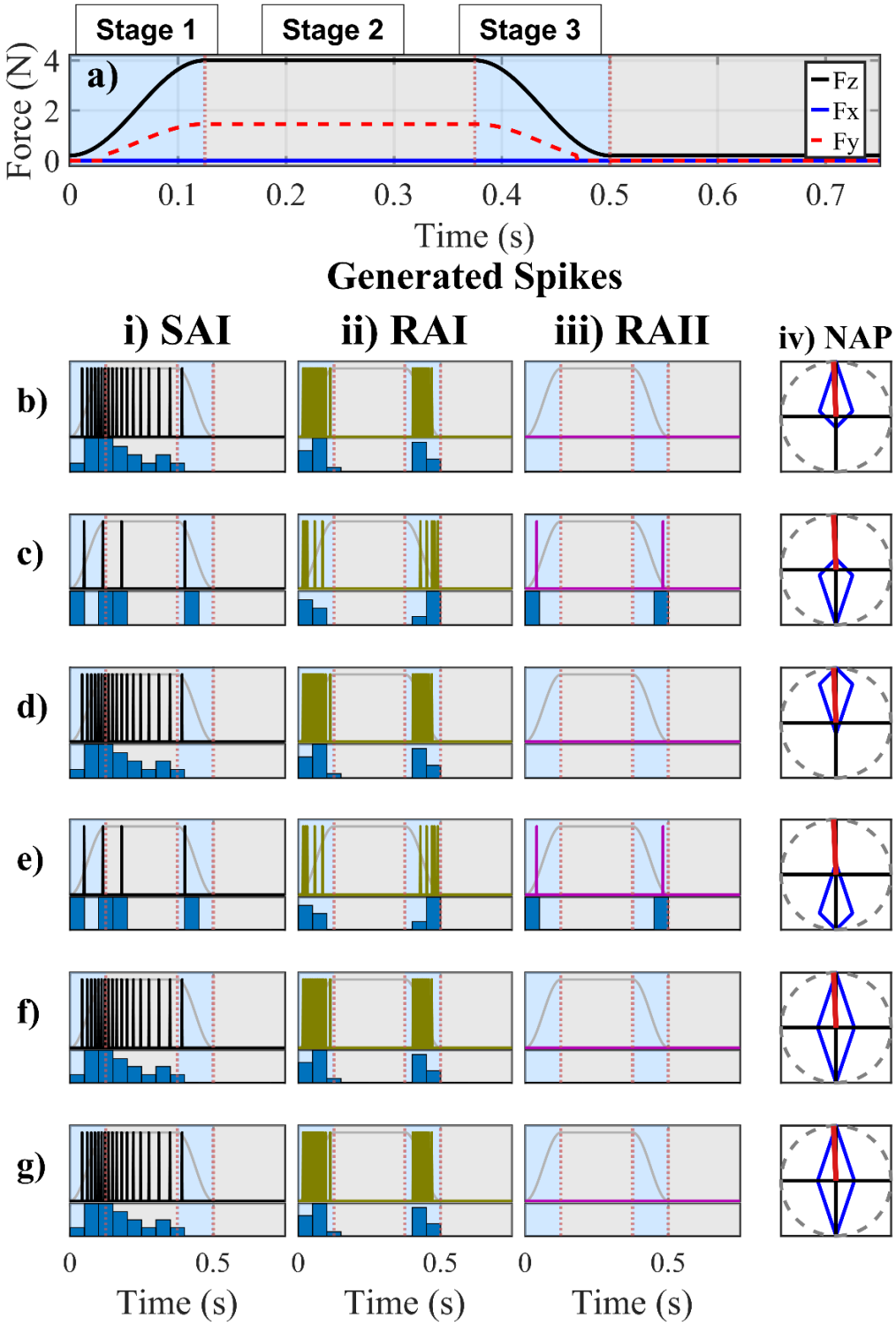

Fig.6 – Synthetic force inputs from [3] (a) and corresponding spike trains for each NAP type under aligned (b, d, f) and misaligned (c, e, g) conditions. Each output subfigure (b-g) depicts the generated spike train for SAI (i), RAI (ii) and RAII (iii)

of force application were lengthened and real-world capabilities considered, giving:

- Stage 1 (5 to 15 second): Initial contact on a surface with pressure only $F_Z(t)$.
- Stage 2 (15 to 25 second): Performing a static pushing along Y direction to generate $F_Y(t)$ and $F_Z(t)$, simultaneously, i.e. $\theta_R(t) = 90$.
- Stage 3 (25 to 30 second): Lift finger off the surface.

Each stage has two periods, first a dynamic period (D) where the change from the previous stage occurs, and then a static stage (S) where the new forces are sustained, as highlighted in Fig. 7(a).

The input forces are designed to produce a constant resultant shear direction of $\theta_R(t) = 90°$ during Step 2. Two tuning angles, θ_T= 75° and 255°, are examined to represent near-alignment and near-unalignment conditions, respectively. Slight offsets from perfect alignment (90°, 270°) allow clearer interpretation of output variations related to NAP geometry. A typical sensitivity value of k = 3 is used to generate spike trains for SAI, RAI, and RAII afferents. Figure 7b–g presents the resulting spike outputs and histograms for each NAP shape. The dataset represents a controlled fingertip press–push–lift action without real-world artefacts such as finger tremor or alignment error.

C: Effect of θ_T

The resulting spike trains, as shown in Fig. 7(b-g), are analyzed by introducing spiking frequency (SF) which is the spike count per second, calculated as an average across the active period. A spike train voltage of 30 mV is used as a threshold to count a neuron firing event, as defined by the Izhikevich Model [21, 22]. SF has a unit of pulses per second

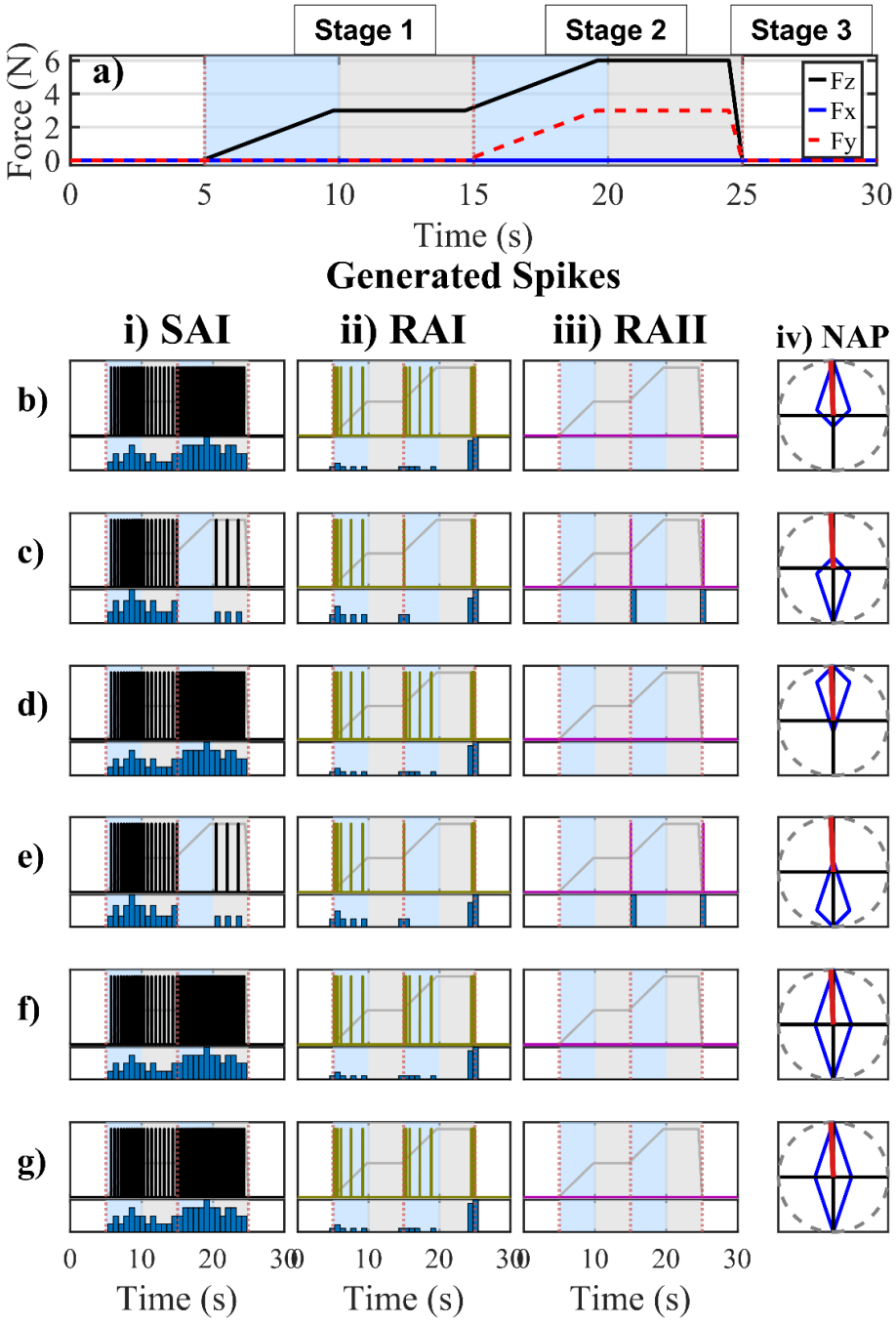

Fig. 7 - Simulated press–push–lift force inputs (a) and corresponding spike trains for each NAP type under aligned (b, d, f) and misaligned (c, e, g) conditions. Each output subfigure (b-g) depicts the generated spike train for SAI (i), RAI (ii) and RAII

(PPS). Spike train responses as a function of θ_T, ranging from 0° to 360°, are evaluated for each NAP as shown in Fig. 8. SF values obtained from DDMM, especially at points where $\theta_R(t)$ is aligned with θ_T, can be compared with those obtained from biological neuron recordings as reported in literature [3,16-18].

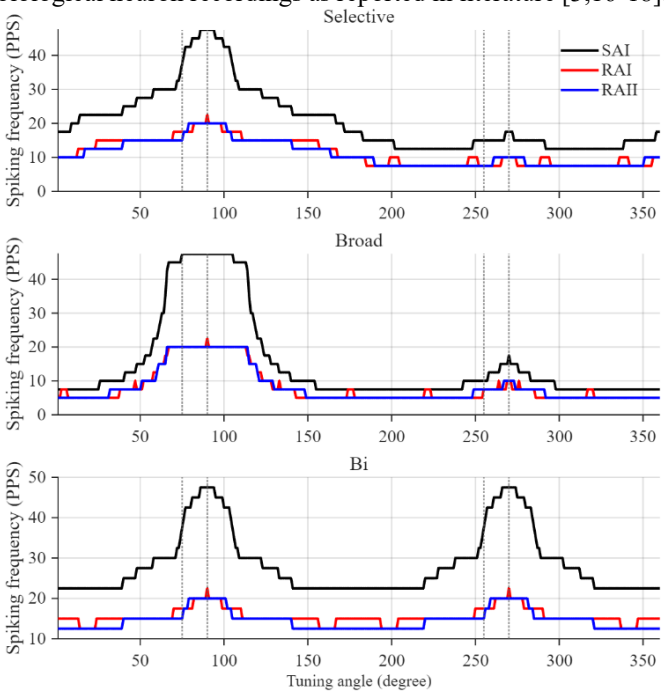

Fig. 8- Spiking frequency (SF) as a function of tuning angle (θ_T) showing direction-dependent responses for a) Selective Uni-Polar, b) Broad Uni-Polar and c) Bi-Polar.

D: Comparison with the CMM

The DDMM not only introduces shear force angles to assist direction tuning, but also implements NAPs, with their effective interaction leading to modeled spikes. We compare the performance of DDMM and CMM by inputting applied force ($F_Z(t)$) only in CMM (Fig. 1), and $F_X(t), F_Y(t), F_Z(t)$ into the DDMM (Fig. 3).

TABLE III - Simulated spiking frequencies (SF) for each afferent type and NAP shape under aligned and misaligned conditions.

	Selective	Broad	Bi	CMM
SAI				
SF (75°)	37.5	47.5	37.5	47.5
SF (255°)	15	10	37.5	47.5
SF Diff	22.5	37.5	0	0
RAI				
SF (75°)	17.5	20	17.5	15
SF (255°)	7.5	7.5	17.5	15
SF Diff	10	12.5	0	0
RAII				
SF (75°)	15	20	15	10
SF (255°)	7.5	7.5	15	10
SF Diff	7.5	12.5	0	0

Table III summarizes all SFs for the different NAPs shown in Fig. 7, and comparison values obtained from corresponding CMM.

V. Experimental Pilot Evaluation

Fig. 9 shows the experiment set up whereby a HE6x6 force plate (AMTI, Watertown, USA) was used to collect multi-axis force data with sample rate of 100 Hz. A healthy participant (female, 28yr) was instructed to conduct the finger press-push-lift actions on the force plate, following steps described in Section IV. The research protocol was reviewed and approved by the ERGO Committee at University of Southampton (ERGO/FEPS/108281). The participant provided written informed consent prior to data collection and were fully informed about the study's objectives and data usage.

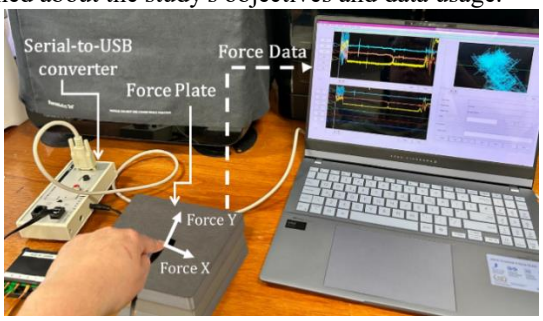

Fig. 9- Experimental setup using an AMTI triaxial force plate for fingertip press–push–lift measurements.

Real time force data plotting was provided to the participant to help maintain pressure ~3N during the push (Stage 2) and ensure shear was static without relative movement between fingertip and the force plate, mimicking biological tests [3, 17]. The test was repeated 5 times, and the mean forces in all three directions, as shown in Fig. 10(a), were used as inputs for the DDMM. Fig. 10(b-g) shows typical spiking trains generated for each NAP profile (selective uni-polar, broad uni-polar and bi-polar) when $\theta_T = 75°$ and $\theta_T = 225°$. Corresponding histograms are also presented underneath each spike train in Fig. 10. Table IV gives the afferent's values for selectivity factor in each case alongside the difference between the cases.

TABLE IV – Experimental spiking frequencies (SF) and differences

	Selective	Broad	Bi	CMM
SAI				
SF (75°)	13.4	16.11	13.05	17.8
SF (255°)	4.5	2.66	13.05	17.8
SF Diff	8.9	13.45	0	0
RAI				
SF (75°)	2.5	3	2.5	3
SF (255°)	1	0.5	2.5	3
SF Diff	1.5	2.5	0	0
RAII				
SF (75°)	1	1.5	0.5	1
SF (255°)	0.5	0	0.5	1
SF Diff	0.5	1.5	0	0

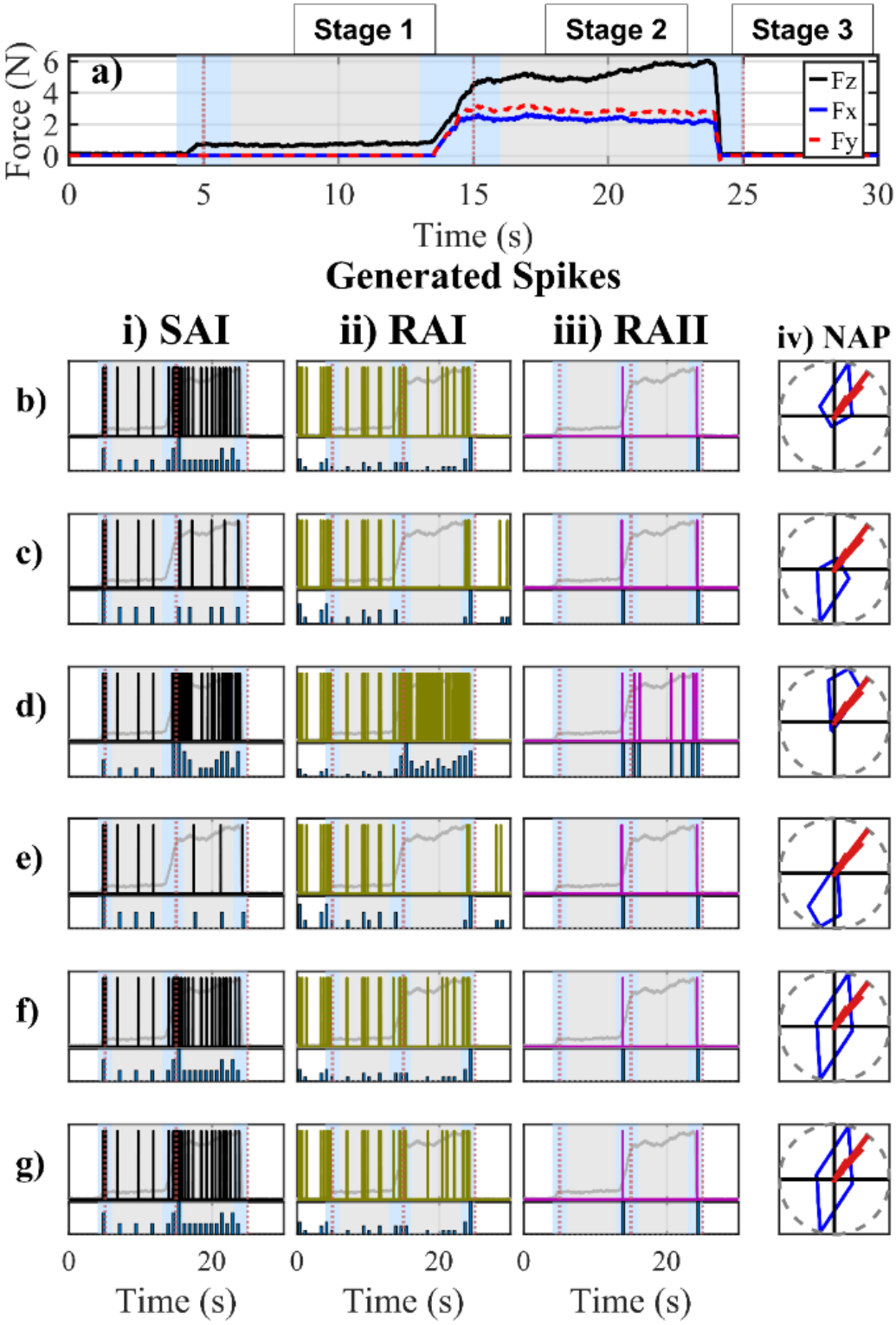

Fig. 10 — Experimental press–push–lift forces (a) and corresponding spike trains for each NAP type under aligned (b, d, f) and misaligned (c, e, g) conditions, showing SAI, RAI, and RAII responses with overlaid resultant shear vectors

VI. Discussion

The DDMM demonstrated clear directional sensitivity, with firing activity closely linked to the alignment between the resultant shear force and the NAP. By incorporating attenuated forces as inputs, the relationship between resultant shear force and each NAP type was established, producing direction-dependent spiking behaviour consistent with natural mechanoreceptive afferent responses [3,16], as illustrated in Figure 6. Among the remaining profiles, as shown in Table II, the selective NAP yielded lower PRSI values (0.31-0.38) and was closest to the reported biological means (0.23, 0.24),

compared with broad NAP. This suggests it may represent the most suitable common profile for modelling afferent directional sensitivity. By comparing the model outputs to recorded microneurography data, increased confidence can be placed in the biological relevance of the DDMM responses.

As shown in Fig. 7, the relationship between expected afferent behaviour and model output aligns closely. The slow adapting neurons (Fig. 7(b–g)(i)) fired during sustained pressure (Stages 2–3), and periods with no shear forces (Stage 1). The rapid adapting neurons (Fig. 7(b–g)(ii)) were active during dynamic loading (Stages 2–3 D), and those sensitive to acceleration responded to pressure changes at the transition points, consistent with biological data [2,4]. As seen in Fig. 7, the DDMM reproduces the expected adaptation behaviour: the slow adapting neurons sustain firing for a longer duration before gradually decreasing, whereas the rapid adapting neurons show a much faster decay in spike rate, consistent with those observed in biological studies [2,4].

Across all afferent types, Stage 1 is shown to be unaffected by directional shears, with the resulting spike trains producing equivalent results across all scenarios. As shown in Fig. 7(c)(iv) the misalignment of the selective uni-polar NAP results in a lower AF(t) than the aligned case (Fig. 7(b)(iv)). The effect of this is seen between Fig. 7(b) and 7(c), where, in comparison to Fig. 7(b), the overall activity of Fig. 6(c) is significantly reduced. Fig. 7(d-e), which show a broad uni-polar NAP, also demonstrate a significant reduction in spiking response between the two cases. The effect of AF(t) is more prevalent in this set-up as the broader tip of the NAP allows for a much higher AF(t) at the near-perfect alignment (Fig. 7(d)(iv)) than that of the selective uni-polar (Fig. 7(b)(iv)). The inverse effect is seen between the unaligned examples (Fig. 7(c)(iv) and Fig. 7(e)(iv)), where the broader base of the selective uni-polar (Fig. 7(c)(iv)) allows for more spiking than the broad counterpart (Fig. 7(e)(iv)). The implication of these results is that the selective uni-polar NAP is better at targeting precise directions of shear but has a higher baseline of activity at unalignment whereas the broad uni-polar profile allows for a general direction to be targeted with very little activity in unaligned cases. The benefits of this are that the broad uni-polar profile can very distinctly depict a general direction of shear, which may be useful for slip detection, whereas the selective uni-polar can distinguish a much more precise shear direction, which may be useful for fine hand manipulation.

When in the near-aligned case for the bi-polar NAP (Fig. 7(f)), the profile exhibits the same response as the selective uni-polar profile, which is expected due to the similarities in NAP shape. However, at the near unaligned case (Fig. 7(g)) the bi-polar profile shows no change in spiking behaviour compared to the near-aligned case. This demonstrates the mirrored aspect of the bi-polar profile, where a 180° rotation makes no difference to AF(t) and hence spike output. One possible use case for this profile shape would be the detection of rubbing, which typically creates shears in alternating 180° directions. The detection of a rubbing sensation is very important for injury prevention such as ulcers, a prevalent issue for people with neuropathy of the foot.

It is evidenced in Fig. 8 that DDMM led to directionally sensitive SF for SAI, RAI and RAII, as the SF varies with θ_T, regardless of NAP. This aligns well with the microneurography recordings as reported by Birznieks et al. [3]. As shown in Fig. 4, maximum AF(t)s are expected at $\theta_T = \theta_R$, which aligns with the observed results in Fig. 7(a-c) where the peak of SF sits at $\theta_T = \theta_R = 90°$, further demonstrating the directional tuning sensitivity of DDMM. The selective uni-polar (Fig. 8(a)) profile shows a steep drop-off rate centered on the true alignment case (90°). In comparison the broad uni-polar NAP (Fig. 8(b)) exhibits a slower drop-off rate centered on the true alignment case (90°). The profile for the bi-polar NAP (Fig. 8(c)) matches the selective uni-polar profile for $0° - 180°$ range after which it is mirrored, representing the bi-polar behavior. Unlike the DDMM directly sensitive SF values, the CMM SF outputs in Table III shows no change in SF between different values of θ_T. Table III shows that there is no difference in SF between SAI spiking behavior for the broad uni-polar NAP and CMM at $\theta_T = 75^{\circ}$, due to an AF(t) of 1 (Fig. 8(b)) making $F_A(t) = F_Z(t)$. This does not carry through to the selective uni-polar and bi-polar NAPs where $AF < 1$ at $\theta_T = 75^{\circ}$, hence $F_A(t) < F_Z(t)$ which therefore produces a lower firing rate. The results for RAI and RAII show a higher SF for all NAPs than the CMM produced. The cause of this is that in suppressing $F_A(t)$ in Stage 1, the transition in Stage 2 Dynamic Period goes from 3N-6N (ΔF_A(10s-15s) = 3N) to 0N-6N (ΔF_A(10s-15s) = 6N), hence eliciting a greater spiking response.

Evaluation based on experimental measurements, as shown in Fig. 9, shows similar stages as for those in Fig. 7. Fig. 10(a), the experimental force data, highlights a key issue with human data. While the participant was instructed to only apply shear in the Y direction, Stage 2 clearly shows the presence of shear in both the X and Y directions. This is due to the difficulty of maintaining static shears produced by the fingertip. It is also worth noting that the experimental data differs from the artificial data in the reduced length of the dynamic period in each stage. Again, this is due to the difficulty in producing constantly changing shears as a human participant. Another key variation is the fluctuations seen in the static stages of Stage 2. Fig. 10(b-g) show the spikes generated using the same NAPs as Fig. 6. The effect of the imprecise shear directions has produced a resultant shear vector at $\sim 45^{\circ}$. In doing so the AF(t) calculated for each NAP (Fig 10(b-g)(iv)) differs slightly from those calculated in Fig. 7.

Fig. 10(b-c) demonstrate the firing result of the experimental forces with a selective uni-polar NAP. Much like the artificial data, no activity is seen during Stage 1 as there is no shear data. Stage 2 across all SAI response (Fig. 10(b-g)(i)) shows a faster decrease in SF in the static shear section. The implication of this is that the static period does not only contain static applied forces. This is confirmed by the spiking activity with the RAI and RAII response (Fig. 10(b-g)(ii–iii)). The variation in both direct pressure and shear forces at this moment has resulted in neural spiking activity in RAI and RAII. As with the artificial data, the relationship between the near aligned and near unaligned cases shows a clear directional dependency. Equally, the relationship between the selective uni-polar and

broad uni-polar still stands. These similarities are further reflected in the results shown in Table IV.

The success of this work opens several exciting avenues for future research. Building on the demonstrated effectiveness of the current model, future developments can incorporate even more sophisticated force application systems with enhanced mechanical precision and real-time feedback control. The model's strong directional sensitivity provides an excellent foundation for expansion, incorporating simultaneous directional and magnitude encoding through multi-modal neuron models or population-level integration schemes.

A particularly promising direction involves combining multiple neural models to create a comprehensive mesh of responses that can perform sophisticated population coding. This approach would leverage the individual directional preferences of multiple neurons to create a robust encoding system capable of representing complex force patterns across the entire tactile surface. Such population-level modeling could significantly enhance the system's ability to encode both directional and magnitude information simultaneously while maintaining the biological fidelity demonstrated in the current work.

The model's proven directional sensitivity and robust response characteristics also provide an ideal platform for advancing prosthetic control applications. By implementing this approach in closed-loop control networks, the directional force encoding could enable more intuitive and precise prosthetic manipulation. The biological relevance of the model's responses suggests that users could develop natural control strategies that leverage their existing neural pathways for tactile feedback, potentially revolutionizing prosthetic hand control and user experience.

VII. Conclusions

This study presented a DDMM that successfully reproduces key aspects of human mechanoreceptor encoding by incorporating directional tuning into the mechanotransduction process. Through artificial force simulations, the model demonstrated that the inclusion of neural attenuation profiles (NAPs) enables spiking activity that varies systematically with shear force direction, reflecting the directional sensitivity reported in biological recordings. Both slow and rapid adapting neuron responses followed expected adaptation patterns, and variations in NAP geometry were shown to modulate tuning sharpness and baseline firing levels. Selective uni-polar profiles captured precise directional sensitivity, broad uni-polar profiles provided coarse but distinct shear detection, and bi-polar profiles accurately represented 180° symmetric force conditions. The physiological validity of the model was further supported by using synthetic force inputs used in [3], with model outputs demonstrating that PSRI values fall within one standard deviation of experimentally observed spike responses.

Experimental validation using human fingertip data further confirmed the DDMM's robustness under realistic, variable loading conditions. Despite natural variability in shear application, the model maintained directional tuning, demonstrating strong agreement between predicted and biologically observed behaviors. This establishes the DDMM as a biologically inspired and computationally efficient framework capable of representing tactile force direction with high fidelity.

Beyond its theoretical contribution, the DDMM provides a foundation for the development of tactile feedback systems that emulate the biological encoding of direction-dependent forces. When integrated with multi-axis force sensors and real-time processing, this framework could serve as the computational core of next-generation prosthetic and robotic tactile interfaces. Its biologically grounded encoding scheme has the potential to enhance closed-loop prosthetic control, enabling users to perceive and regulate directional forces naturally, thereby improving manipulation accuracy and embodiment.

Future work will focus on extending the DDMM toward population-level modelling, allowing multiple neuron models with distinct NAPs to operate collectively for distributed encoding of complex tactile inputs. Incorporating additional biological data on mechanoreceptor density and spatial organization could further improve realism and predictive power. Finally, validation using a broader participant pool and more diverse interaction tasks, such as sliding and rotational contacts, will be essential to demonstrate generalizability and guide translation to practical neuroprosthetics and robotic applications.

DATA AVAILABILITY STATEMENT

All data supporting this study are openly available from the University of Southampton repository at DOI https://doi.org/10.5258/SOTON/D3758

ACKNOWLEDGMENT

Hope O. Shaw acknowledges the support of the UK Engineering and Physical Sciences Research Council (EPSRC) grant number EP/S02249X/1 for the Centre for Doctoral Training in Prosthetics and Orthotics to provide PhD studentship.

References

[1] J. Ochoa and E. Torebjörk, "Sensations evoked by intraneural microstimulation of single mechanoreceptor units innervating the human hand," *The Journal of physiology,* vol. 342, no. 1, pp. 633-654, 1983.

[2] R. S. Johansson and Å. B. Vallbo, "Tactile sensory coding in the glabrous skin of the human hand," *Trends in neurosciences,* vol. 6, pp. 27-32, 1983.

[3] I. Birznieks, P. Jenmalm, A. W. Goodwin, and R. S. Johansson, "Encoding of Direction of Fingertip Forces by Human Tactile Afferents," *The Journal of*

Neuroscience, vol. 21, no. 20, pp. 8222-8237, 2001, doi: 10.1523/jneurosci.21-20-08222.2001.

[4] K. O. Johnson, "The roles and functions of cutaneous mechanoreceptors," *Current opinion in neurobiology,* vol. 11, no. 4, pp. 455-461, 2001.

[5] H. Bajwa and Y. Al Khalili, "Physiology, vibratory sense," 2019.

[6] F. Cordella *et al.*, "Literature review on needs of upper limb prosthesis users," *Frontiers in neuroscience,* vol. 10, p. 209, 2016.

[7] A. Chadwell, L. Kenney, S. Thies, A. Galpin, and J. Head, "The reality of myoelectric prostheses: understanding what makes these devices difficult for some users to control," *Frontiers in neurorobotics,* vol. 10, p. 7, 2016.

[8] K. C. de Almeida Lima, L. da Silva Borges, E. Hatanaka, L. C. Rolim, and P. B. de Freitas, "Grip force control and hand dexterity are impaired in individuals with diabetic peripheral neuropathy," *Neuroscience letters,* vol. 659, pp. 54-59, 2017.

[9] A. L. Ciancio *et al.*, "Control of prosthetic hands via the peripheral nervous system," *Frontiers in neuroscience,* vol. 10, p. 116, 2016.

[10] C. M. Oddo *et al.*, "Intraneural stimulation elicits discrimination of textural features by artificial fingertip in intact and amputee humans," *elife,* vol. 5, p. e09148, 2016.

[11] N. Hale, M. Valero, J. Tang, D. Moser, and L. Jiang, "A preliminary study on characterisation of finger interface kinetics using a pressure and shear sensor system," *Prosthetics & Orthotics International,* vol. 42, no. 1, pp. 60-65, 2018, doi: 10.1177/0309364617728121.

[12] D. Deflorio, M. Di Luca, and A. M. Wing, "Skin and Mechanoreceptor Contribution to Tactile Input for Perception: A Review of Simulation Models," *Frontiers in Human Neuroscience,* vol. 16, 2022, doi: 10.3389/fnhum.2022.862344.

[13] M. Rasouli, Y. Chen, A. Basu, S. L. Kukreja, and N. V. Thakor, "An Extreme Learning Machine-Based Neuromorphic Tactile Sensing System for Texture Recognition," *IEEE Transactions on Biomedical Circuits and Systems,* vol. 12, no. 2, pp. 313-325, 2018, doi: 10.1109/tbcas.2018.2805721.

[14] F. L. A. Macdonald, N. F. Lepora, J. Conradt, and B. Ward-Cherrier, "Neuromorphic Tactile Edge Orientation Classification in an Unsupervised Spiking Neural Network," *Sensors*, vol. 22, no. 18, doi: 10.3390/s22186998.

[15] Q. Ouyang, J. Wu, Z. Shao, D. Chen, and J. W. Bisley, "A Simplified Model for Simulating Population Responses of Tactile Afferents and Receptors in the Skin," *IEEE Transactions on Biomedical Engineering,* vol. 68, no. 2, pp. 556-567, 2021, doi: 10.1109/tbme.2020.3007397.

[16] M. Valero *et al.*, "Interfacial pressure and shear sensor system for fingertip contact applications," *Healthcare Technology Letters,* vol. 3, no. 4, pp. 280-283, 2016, doi: 10.1049/htl.2016.0062.

[17] P. Fortier-Poisson, J.-S. Langlais, and A. M. Smith, "Correlation of fingertip shear force direction with somatosensory cortical activity in monkey," *Journal of Neurophysiology,* vol. 115, no. 1, 2015 Oct 14, doi: 10.1152/jn.00749.2014.

[18] P. J. Fitzgerald, J. W. Lane, P. H. Thakur, and S. S. Hsiao, "Receptive Field Properties of the Macaque Second Somatosensory Cortex: Representation of Orientation on Different Finger Pads," *Journal of Neuroscience,* vol. 26, no. 24, pp. 6473-6484, 2006, doi: 10.1523/jneurosci.5057-05.2006.

[19] S. Ruiz, P. Crespo, and R. Romo, "Representation of moving tactile stimuli in the somatic sensory cortex of awake monkeys - PubMed," *Journal of neurophysiology,* vol. 73, no. 2, 1995 Feb, doi: 10.1152/jn.1995.73.2.525.

[20] E. K. Kim, S. A. Wellnitz, S. M. Bourdon, E. A. Lumpkin, and G. J. Gerling, "Force sensor in simulated skin and neural model mimic tactile SAI afferent spiking response to ramp and hold stimuli," *Journal of NeuroEngineering and Rehabilitation,* vol. 9, no. 1, p. 45, 2012, doi: 10.1186/1743-0003-9-45.

[21] E. M. Izhikevich, "Simple model of spiking neurons," *IEEE Transactions on neural networks,* vol. 14, no. 6, pp. 1569-1572, 2003.

[22] E. M. Izhikevich, "Which model to use for cortical spiking neurons?," *IEEE transactions on neural networks,* vol. 15, no. 5, pp. 1063-1070, 2004.

[23] J. Kim, Y. I. Choi, J.-w. Sohn, S.-P. Kim, and S. J. Jung, "Modeling long-term spike frequency adaptation in sa-i afferent neurons using an izhikevich-based biological neuron model," *Experimental Neurobiology,* vol. 32, no. 3, p. 157, 2023.

[24] D. Esposito *et al.*, "A neuromorphic model to match the spiking activity of Merkel mechanoreceptors with biomimetic tactile sensors for bioengineering applications," *IEEE Transactions on Medical Robotics and Bionics,* vol. 1, no. 2, pp. 97-105, 2019.